



Magnetic fluorinated mesoporous $g\text{-C}_3\text{N}_4$ for photocatalytic degradation of amoxicillin: Transformation mechanism and toxicity assessment

Amir Mirzaei, Zhi Chen, Fariborz Haghishat*, Laleh Yerushalmi

Department of Building, Civil and Environmental Engineering (BCEE), Faculty of Engineering & Computer Sciences, Concordia University, Montreal, Quebec, Canada



ARTICLE INFO

Keywords:
Photocatalyst
 $g\text{-C}_3\text{N}_4$
Magnetic
Amoxicillin
Toxicity
By-products
Exfoliation

ABSTRACT

A novel fluorinated graphitic carbon nitride photocatalyst with magnetic properties was synthesized by a facile hydrothermal method and used for degradation of amoxicillin (AMX) in water. Compared to the bulk $g\text{-C}_3\text{N}_4$, magnetic fluorinated $\text{Fe}_3\text{O}_4/g\text{-C}_3\text{N}_4$ (FeGF) with a high specific surface area ($243\text{ m}^2\text{ g}^{-1}$) and easy separation from aqueous solution by magnet, led to improved photocatalytic activity in terms of AMX removal and mineralization as well as detoxification of the solution. The results showed that in comparison with a 500 W visible lamp, using a UV lamp (10 W) was considerably more effective for AMX removal, its mineralization and detoxification of the solution. Based on the measurement of accurate mass of the transformation products and their main fragments, a degradation pathway for AMX was proposed. The peak intensities of most transformation products (TPs) generated by using modified photocatalyst under UV light (UV/FeGF2) process were significantly lower than those generated by using pristine $g\text{-C}_3\text{N}_4$, suggesting that UV/FeGF2 process produced a higher extent of mineralization and a lower accumulation of transformation by-products. Based on the use of inexpensive precursor and modifier, simple preparation, good photocatalytic activity and low energy consumption, the proposed method can guide the development of low-cost and high-performance photocatalysts.

1. Introduction

Every year about 100,000–200,000 tons of antibiotics are used for the treatment of bacterial infections of humans and animals worldwide [1]. The presence of antibiotics in aquatic media is of global concern due to their potential effects on human and natural ecosystems and the development of pathogen resistance to antibiotics even at trace concentrations [2,3]. Amoxicillin (AMX) is a widely used β -lactam antibiotic in human and veterinary medicine [4]. About 65% of the global antibiotic market belongs to β -lactam antibiotics [5]. However, after the oral administration of a dose of 500 mg, approximately $86 \pm 8\%$ of AMX is excreted in the urine within two hours of consumption due to the slow rate of metabolism [2]. Unfortunately, most antibiotics such as AMX are recalcitrant to conventional biological wastewater treatment processes [4,6]. Due to the high consumption and low metabolic degradation, AMX is often detected at the concentration range of ng/L to $\mu\text{g/L}$ in water bodies [7]. Alygizakis et al. [8] examined the Eastern Mediterranean Sea and reported that among 38 detected pharmaceuticals, AMX with up to 127.8 ng/L showed the highest concentration level.

Photocatalytic degradation of organic compounds has been identified as a promising technique, as it may lead to the mineralization of

contaminants into carbon dioxide, water and mineral acids without using chemicals or generating sludge [9–12]. When a photocatalyst is irradiated by light with the energy equal to or greater than its band gap, it causes the generation of free electrons in the conduction band, leaving behind holes or electron vacancies in the valence band [13,14]. A list of reactions which may contribute to the photocatalytic process can be found elsewhere [15]. TiO_2 and ZnO are among the most widely used photocatalysts for degradation of antibiotics in water due to their non-toxicity, chemical inertness, and low cost [2,12,15,16]. However, TiO_2 and ZnO have no visible-light response due to their large band gap which restricts their applications [16]. Therefore, it is not surprising that recently many studies have focused on the visible-driven photocatalyst, as the visible light constitutes a large proportion of solar light [17]. Since the report of photocatalytic activity of $g\text{-C}_3\text{N}_4$ by Wang et al. [18], this process has attracted growing attention due to its unique characteristics, including the appropriate position of valence and conduction bands, inexpensive precursors, facile synthesis processes, non-toxicity, high chemical stability and resistant to photocorrosion [9,12,16,17,19,20].

Nevertheless, the low specific surface area, high recombination rate of electrons and holes and negligible absorption above 460 nm are the main limitations of $g\text{-C}_3\text{N}_4$, causing its low photoactivity and its limited

* Corresponding author.

E-mail address: haghi@bcee.concordia.ca (F. Haghishat).

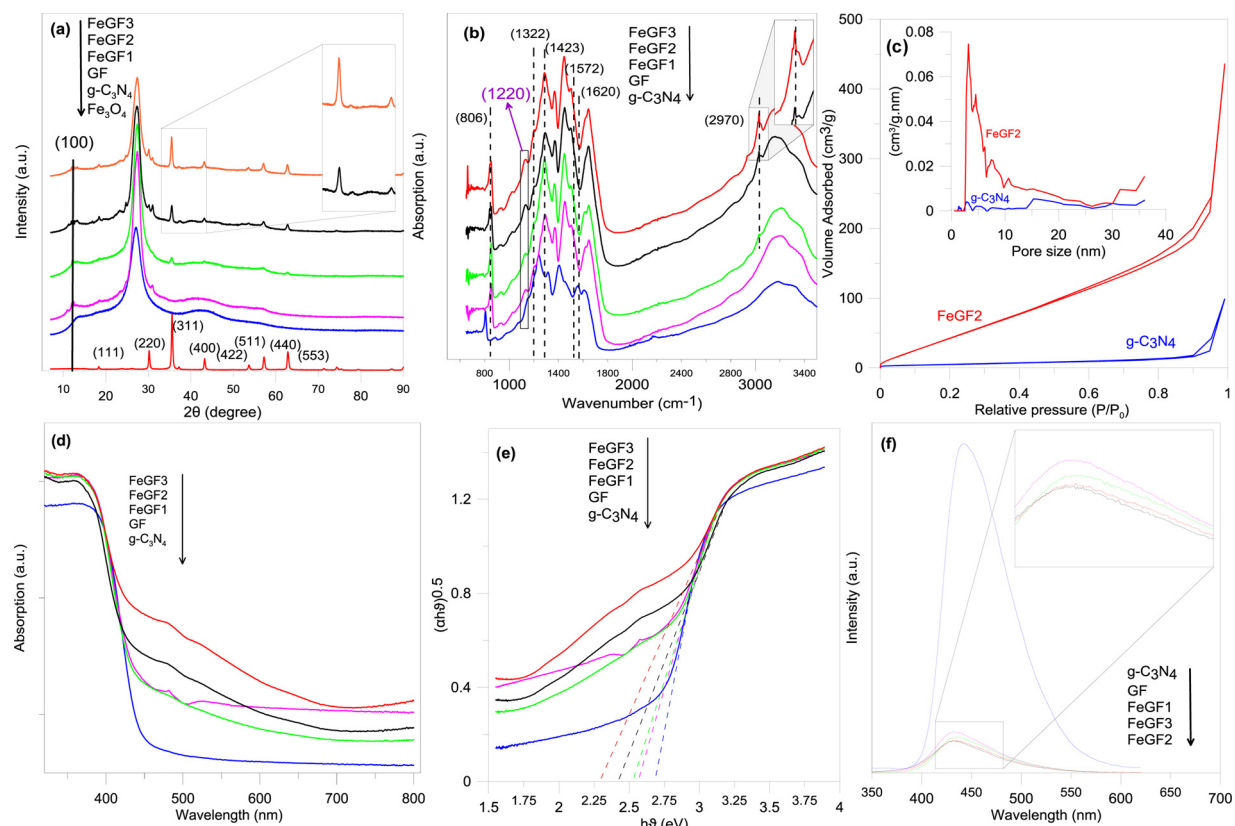


Fig. 1. (a) XRD patterns, (b) FTIR spectra, (c) Nitrogen adsorption–desorption isotherms (inset: pore size distribution), (d) UV–vis diffuse reflectance spectra, (e) Band gaps (E_g), (f) PL emission spectra of $g\text{-C}_3\text{N}_4$, GF, FeGF1, FeGF2 and FeGF3.

application as a standalone photocatalyst [9,12,21]. Moreover, difficulty in the separation and recovery of photocatalysts from the treated solution and the potential loss of the suspended particulate catalysts in the process of photocatalytic reaction limit its application [16]. To date, various strategies have been applied to enhance the photocatalytic activity of $g\text{-C}_3\text{N}_4$. For instance, Wang et al. [22] drastically enhanced the photocatalytic activity of $g\text{-C}_3\text{N}_4$ by fluorination, leading to hydrogen evolution and oxidation of benzene to phenol. Wang et al. [23] enhanced the specific surface area by preparing mesoporous $g\text{-C}_3\text{N}_4$, which led to the high selective oxidation of cycloalkanes. Zhang et al. [17] prepared exfoliated $g\text{-C}_3\text{N}_4$ nanosheets with high specific surface area via an acid-assisted hydrothermal method. Although exfoliated $g\text{-C}_3\text{N}_4$ nanosheets show high water dispersion stability which is beneficial for photocatalytic activity, it is very inconvenient to separate and recycle these particles from water [24]. Zhang et al. [16] prepared magnetic $g\text{-C}_3\text{N}_4$ for easy separation of particles from the solution and increased its photocatalytic activity up to 6.4 times compared to that of bare $g\text{-C}_3\text{N}_4$. A few studies have also reported the beneficial effect of $g\text{-C}_3\text{N}_4$ when used as composite with other semiconductors such as Ag/TiO_2 [25] and $\text{MnFe}_2\text{O}_4/\text{graphene}$ [26] for photocatalytic degradation of AMX.

Inspired by the abovementioned studies, a fluorinated porous $g\text{-C}_3\text{N}_4$ with high surface area and magnetic properties was synthesized as a low-cost photocatalyst to remove AMX antibiotic by a cylindrical photoreactor using a low energy-consuming UV-C lamp. Besides the removal and mineralization of AMX, the toxicity of treated solutions were evaluated and compared with the obtained results of using visible light. The generated intermediate products during the processes were identified by using LC-HR-MS/MS method. Accordingly, a mechanism was proposed for the photocatalytic degradation of AMX, and the reusability of photocatalyst in cyclic operations was evaluated.

2. Experimental

2.1. Chemicals

All reagents were analytical grade and were used as received. Urea, ammonium fluoride, *tert*-butyl alcohol (TBA) and ethanol were supplied by Fisher Scientific (ON, Canada). EDTA disodium salt and p-benzoquinone (BQ) were purchased from Alfa-Aesar, USA. Amoxicillin, FeCl_3 , and $\text{FeCl}_2\cdot 4\text{H}_2\text{O}$ were purchased from Sigma-Aldrich, USA. Low range nitrate, nitrite and fluoride ion kits as well as Toxtrac™ kit were supplied by HACH Co. USA. Deionized Milli-Q water (DIW) ($18\text{ }\mu\text{S cm}^{-1}$) was used throughout this study for the preparation of photocatalysts and during the experiments. HPLC-grade formic acid and acetonitrile (Fluka) were used for HPLC analyses.

2.2. Synthesis of photocatalysts

The *in situ* growth of Fe_3O_4 nanoparticles on exfoliated porous $g\text{-C}_3\text{N}_4$ nanosheets was used in this study. Accordingly, carbon nitride ($g\text{-C}_3\text{N}_4$) was synthesized by heating urea up to $550\text{ }^\circ\text{C}$ for 4 h [19]. Fluorinated $g\text{-C}_3\text{N}_4$ nanosheets were prepared by acid-assisted exfoliation of $g\text{-C}_3\text{N}_4$ as follow: (2 g) $g\text{-C}_3\text{N}_4$ was added into 150 mL DIW containing (4 g) NH_4F and then transferred into a 200 mL Teflon-lined autoclave and heated to $180\text{ }^\circ\text{C}$ for 12 h. After cooling to room temperature, the photocatalyst was retrieved, washed and dried at $60\text{ }^\circ\text{C}$ overnight, and was labeled as GF. Magnetic fluorinated $g\text{-C}_3\text{N}_4$ (FeGF1) was prepared according to Ref. [27] with a minor modification. Briefly, GF powder (2 g) was added to 150 mL of ethanol/water (v/v = 1:1) and was sonicated for 10 min. Then, $\text{FeCl}_2\cdot 4\text{H}_2\text{O}$ (1 mmol) and FeCl_3 (2 mmol) were added into the solution and were mixed for 30 min at $60\text{ }^\circ\text{C}$. Afterward, 15 mL ammonia solution was quickly added to the mixed solution and was continuously stirred for 30 min. The prepared

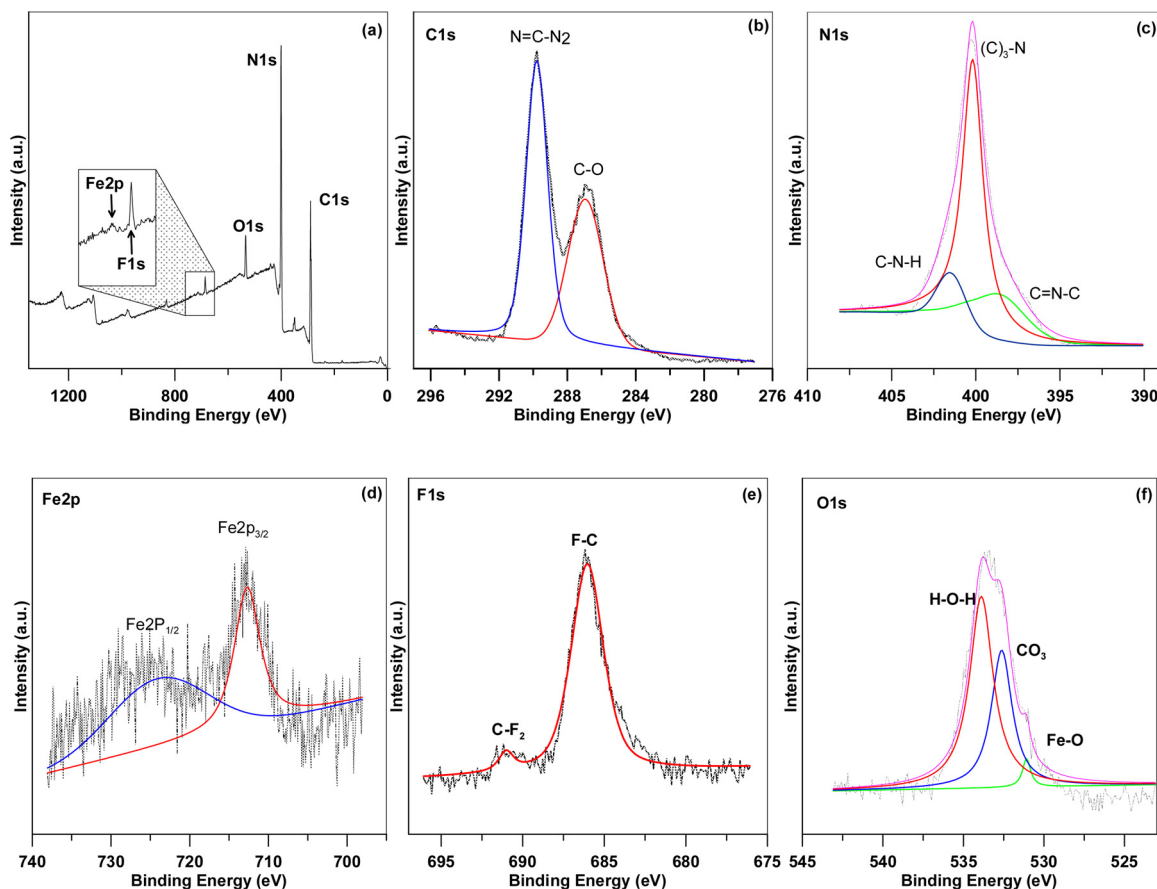


Fig. 2. XPS survey spectra (a), high-resolution XPS spectra of the C1s (b), N1s (c), Fe2p (d), F1s (e) and O1s region (f) of FeGF2.

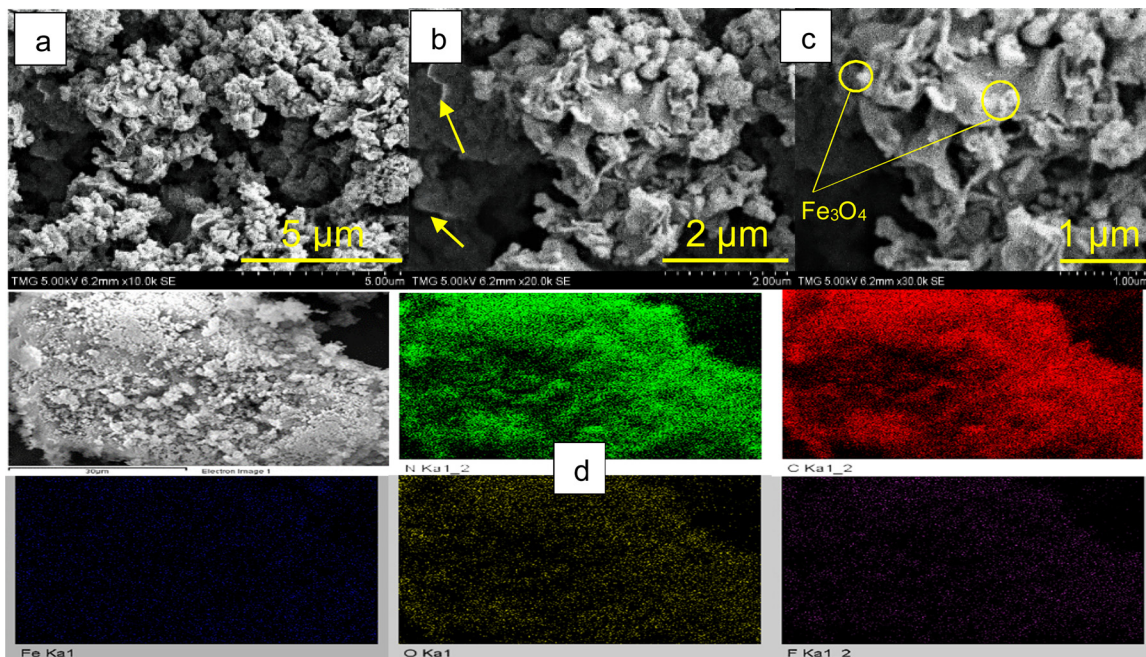


Fig. 3. (a–c) SEM images of FeGF2 sample at different magnifications, (d) elemental mapping of N, C, Fe, O and F of FeGF2.

particles were separated by magnet and were rinsed several times with ethanol and DIW and, then the particles were dried at 60 °C overnight. The photocatalysts prepared by using 2 and 3 mmol $\text{FeCl}_2 \cdot 4\text{H}_2\text{O}$ were designated as FeGF2 and FeGF3, respectively. Pure Fe_3O_4 was synthesized using a similar process as FeGF, but in the absence of GF.

2.3. Characterization of photocatalysts

The crystallinity of as-synthesized samples was characterized using XRD with a Bruker D8 Advance X-ray diffractometer with $\text{Cu K}\alpha$ radiation ($\lambda = 1.5406 \text{ \AA}$) in the 2θ range from 10° to 80°. Fourier

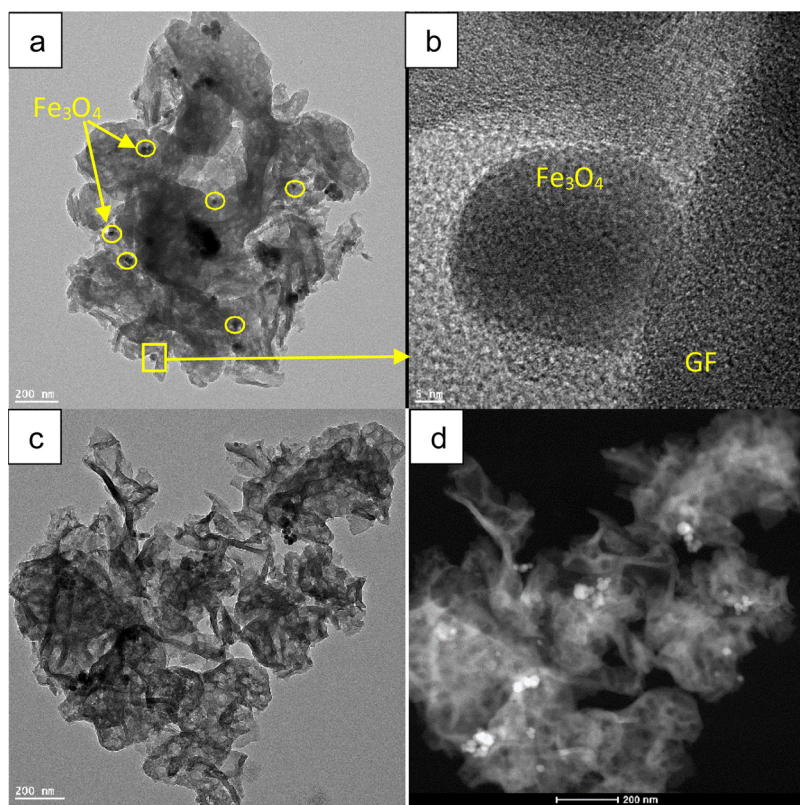


Fig. 4. (a–c) TEM images of FeGF2 sample, (d) high angle annular dark field (HAADF) STEM image of FeGF2.

Transform Infrared (FTIR) spectroscopy was performed by using Thermo Scientific Nicolet 6700 spectrometer (USA). An emission scanning electron microscope (Hitachi S-3400 N) equipped with energy-dispersive spectroscopy (EDS) was used for taking scanning electron microscopy (SEM) and elemental mapping. The transmission electron microscopy (TEM) images were taken by using a Tecnai F20 S/TEM operated at 200 kV. X-ray photoelectron spectroscopy (XPS) was used for the characterization of photocatalysts after fluorination by using Thermo Scientific K-alpha™ spectrometer (USA) equipped with an Al K α X-ray source (1486.6 eV, 0.843 nm) and X-ray spot size of 400 μ m in diameter. Ultraviolet-visible (UV-vis) spectroscopy was performed by a Lambda 750, PerkinElmer (USA) equipped with an integrating sphere. The specific surface area of the photocatalysts was measured by BET method (Autosorb-1, Quantachrome, USA). Photoluminescence spectra were taken by using a spectrofluorimeter, Perkin Elmer, LS45, USA. The magnetic properties of samples were measured by using a Vibrating Sample Magnetometer (VSM, model EV9, ADE Technologies). An atomic absorption spectrophotometer (PinAAcle 900F, PerkinElmer, USA) was used for the measurement of iron ions concentration in the solution.

2.4. Photocatalysis experiments

The photocatalytic experiments with UV and visible light were performed in batch mode of operation. The schematic diagram of UV-driven cylindrical photoreactor can be found in our previous work [13]. A 500 W halogen lamp with a UV cutoff filter (> 400 nm) was used as the light source in visible-driven experiments. In both UV and visible-driven experiments, photocatalysts at 1 g/L concentration were used and the pH of solution was adjusted to 7. Millipore Milli-Q deionized water (DIW) was used to prepare AMX solution at 0.25 mM initial concentration, and air at 1.5 L/min flowrate was bubbled into the solution. The solution temperature was maintained at 25 °C by using a cooling water system. Before irradiation, the solution was circulated for

60 min to ensure the achievement of adsorption/desorption equilibrium. To evaluate the removal efficiency and the extent of mineralization of AMX, 10 mL of solution at different intervals was taken and filtered through 0.22 μ m filter paper to determine the AMX concentration. A similar operation was conducted for cyclic experiments under the UV light.

2.5. Analytical measurements and by-products identification

The removal efficiencies of AMX, and TOC at different time intervals were determined based on Eq. (1):

$$R(\%) = \left(1 - \frac{x_t}{x_0}\right) \times 100 \quad (1)$$

where R (%) is the percentage AMX or TOC removal. x_t is the concentration of AMX (mM) or TOC (mg/L) at time t and x_0 is the initial concentration of AMX or TOC. The transformation products (TPs) of AMX degradation were identified by LC-HR-MS/MS method. Accordingly, samples were injected (1 μ L) into a Phenomenex Kinetex C18 column (2.1 \times 50 mm, 1.7 μ m), using a Nexera UHPLC system (Shimadzu, Columbia, MD). The mobile phases were (A) water with 0.1% formic acid and (B) acetonitrile with 0.1% formic acid at the flow rate of 0.3 mL/min. A linear gradient was used starting with 3% (B), and changing to 85% (B) in 8 min. The column temperature was 40 °C. The MS and MS/MS spectra were collected on a hybrid quadrupole-time-of-flight (QqTOF) TripleTOF 5600 mass spectrometer (SCIEX, Concord, ON, Canada) equipped with a DuoSpray ion source in positive ion mode set at 5 kV source voltage, 450 °C source temperature, and 50 psi for GS1/GS2 gas flows. Data were acquired in IDA (information-dependent acquisition) mode, with a survey TOF-MS acquisition from m/z 80–925, followed by MS/MS on the 3 most intense ions from m/z 200–450 with dynamic background subtraction (DBS) with a total cycle time of 1.0 s. The MS/MS analysis of precursor ions was performed at the collision energy of 30 \pm 10 V. The data were analyzed qualitatively with

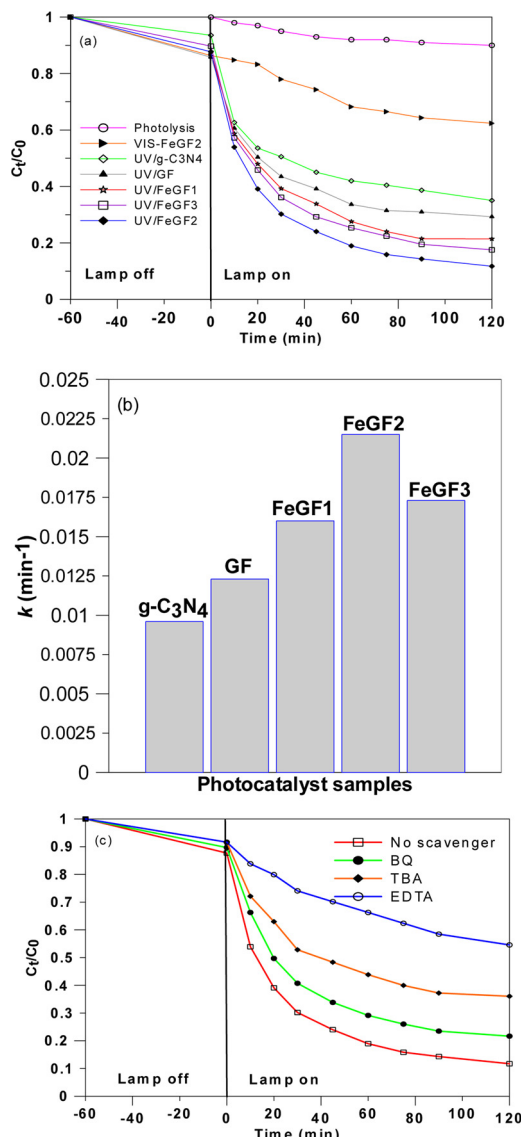


Fig. 5. (a) Photocatalytic activity of photocatalysts for the degradation of AMX under UV and visible light, (b) apparent first-order rate constant, (c) species-trapping experiments for degradation of AMX by FeGF2 photocatalysts; experimental condition: $[AMX]_0 = 0.25$ mM, pH 7, [photocatalyst] = 1 g/L, [scavenger]₀ = 2.5 mM, airflow rate = 1.5 L/min.

PeakView v2.2 and quantitatively with MultiQuant v3.02.

2.6. Toxicity assessment

The antibacterial activity assays of solutions before and after photocatalytic treatments were conducted to evaluate the impact of applied processes on the reduction of solution toxicity. In the first method [28], petri dishes were prepared by mixing appropriate amounts of nutrient broth and agar, followed by boiling the mixture and allowing the formation of gel for at least 1 h. Approximately 50 μ L of *E. coli* ($\sim 1 \times 10^8$ CFU/mL) from a stock solution was subsequently spread over the surface of the agar. A control experiment was conducted using agar made by irradiated water in photocatalytic experiment for 2 h in order to ensure that the observation is due to the antibiotic degradation rather than probable leachate of catalyst and/or a change in the water chemistry. The treated solutions by UV/g-C₃N₄, UV/FeGF2 and Vis/FeGF2 processes after 1 and 2 h were also used for preparation of agar and assessment of changing the toxicity by examined processes. After incubation overnight at 37 °C, the growth of *E. coli* on prepared agars

was noticed. Agar-well diffusion method was also utilized to visualize the change of toxicity before and after the treatment [13]. In this method, after the streaking of agar surface by *E. coli*, three holes with the diameter of ~5 mm were punched into the agar and 50 μ L of solution was introduced into the wells. The petri dishes were placed in incubator at 37 °C overnight to promote the formation of inhibition zone around the wells. A commercial toxicity test kit (Toxtrac™, HACH, USA) was also utilized to quantitatively assess the toxicity in the term of percentage inhibition (PI) of samples according to the manufacturer's protocol. The inhibition of *E. coli* strain was calculated by Eq. (2) [6]:

$$\% \text{ Inhibition} = (1 - \frac{\Delta A_{\text{sample}}}{\Delta A_{\text{control}}}) \times 100 \quad (2)$$

where: ΔA = (initial absorbance value) – (final absorbance value) at 603 nm.

3. Results and discussion

3.1. Structural analysis

Fig. 1(a) shows the XRD patterns of Fe₃O₄, bare g-C₃N₄, and nanocomposites with different Fe₃O₄ contents. The peaks at $2\theta = 18.3^\circ$, 30.2° , 35.6° , 43.2° , 53.6° , 57.1° , 62.6° and 74.2° are indexed as (111), (220), (311), (400), (422), (511), (440), and (553) planes of magnetite (JCPDS: 19-0629) [29]. These sharp narrow peaks indicate that Fe₃O₄ is highly crystalline. For the bare g-C₃N₄, the small peak at 13.2° corresponds to the tri-s-triazine unit plane (100) [30], while the peak at 27.6° is indexed to the (200) plane which arises from the interlayer-stacking of the conjugated aromatic segments [31]. Both corresponding peaks of GF are sharper than that of bare g-C₃N₄. This is due to the rearrangement of g-C₃N₄ structure during the hydrothermal exfoliation process [31,32]. Moreover, as shown in Fig. S1, the (002) peak of g-C₃N₄ is shifted from 27.1° to 27.6° , indicating a decreased gallery distance between the layers during the hydrothermal process [33]. This happens because during the NH₄F-assisted exfoliation, strong acid (HF) is produced by the hydrolysis of NH₄F which leads to the cleavage of g-C₃N₄ layers. The cleavage of g-C₃N₄ layers by strong acids such as HCl [17,33,34] and H₃PO₄ [35] has been reported before. Compared with the pure counterparts, the XRD patterns of FeGF composites contain the peaks of both Fe₃O₄ and g-C₃N₄, and the intensity of Fe₃O₄ peaks gradually increases with the increasing of Fe₃O₄ content. At a higher Fe₃O₄ percentage (**Fig. 1**, FeGF2 and FeGF3) even the weak peaks of Fe₃O₄, such as those in the (400) and (511) planes are detectable (the enlarged image of **Fig. 1(a)**). This indicates that Fe₃O₄ has been successfully introduced into the g-C₃N₄ structure and both are in good combination in the composites.

Fig. 1(b) shows the FTIR spectra of bare g-C₃N₄, GF and FeGF composites. In all samples, the band at 806 cm⁻¹ corresponds to the breathing mode of triazine units [30]. The absorption band at 1620 cm⁻¹ is attributed to C=N stretching [36], while the peaks at 1322, 1423 and 1572 cm⁻¹ can be attributed to the stretching modes of aromatic C–N [37]. As shown, all these peaks shifted to a higher wavelength after fluorination, indicating the strong interaction between the fluorine element and the s-triazine ring. The broad bands at around 3100 cm⁻¹ are related to the N–H stretching vibration modes [38] which indicates that the amino functional group still existed in all samples [39]. The broad bands at 3200–3600 cm⁻¹ correspond to the physically adsorbed H₂O molecules [30]. A peak at 2970 cm⁻¹ is observed for the FeGF composites and its intensity is increased by increasing the Fe₃O₄ content of composites which results from the C–H vibration [40]. As shown in **Fig. 1(b)**, the fluorination of g-C₃N₄ led to the formation of a new band at 1220 cm⁻¹, which is related to the stretching mode of C–F bond [22]. **Fig. 1(c)** shows the N₂ adsorption–desorption isotherms and pore size distribution of g-C₃N₄ and FeGF2 samples. As seen, both isotherms are recognized as type IV with the hysteresis loop. The BET surface area of FeGF2 sample was

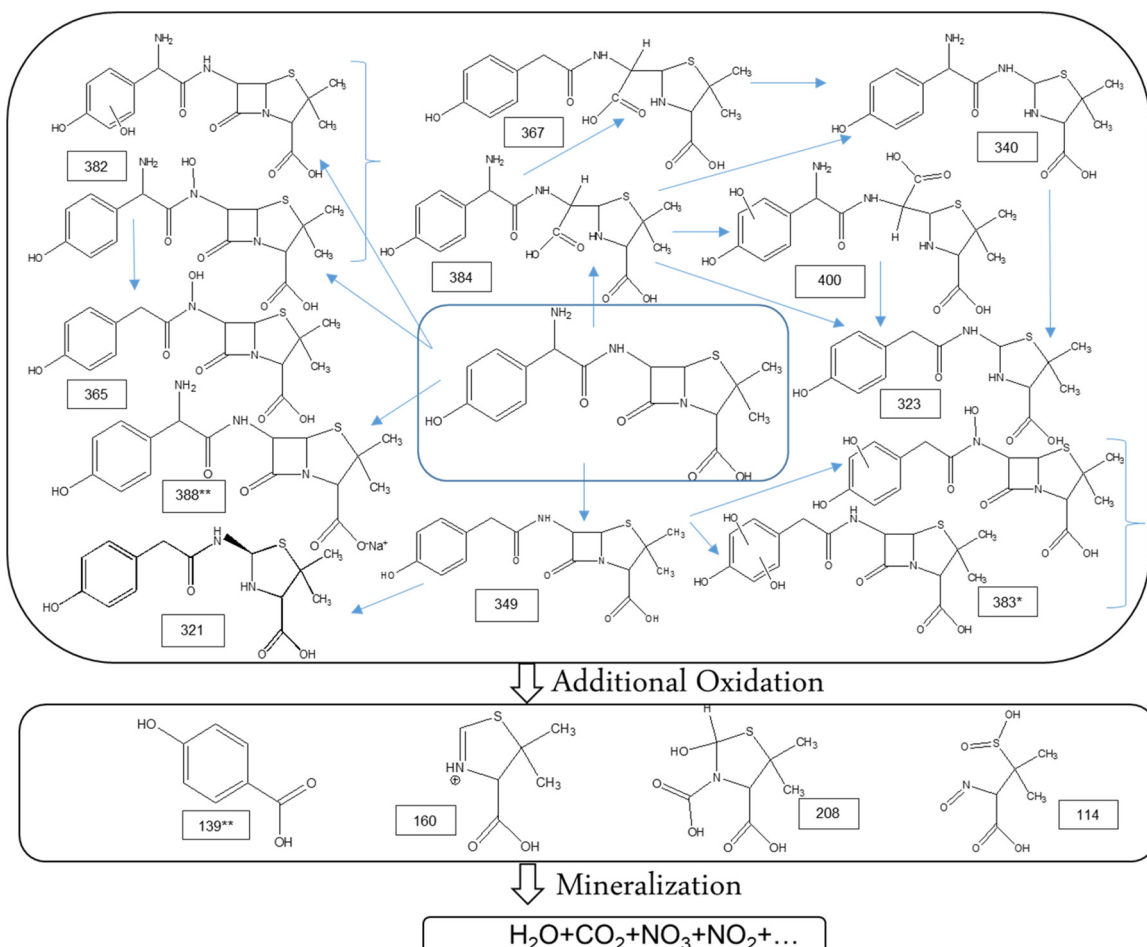


Fig. 6. Schematic diagram of the proposed photocatalytic degradation mechanisms of AMX under UV light. The transformation products (TPs) marked with (*) were detected during UV/g-C₃N₄ process and TPs marked with (**) were detected during UV/FeGF2 processes.

242.71 m²/g which is about 6 times higher than that of bare g-C₃N₄ with 37.85 m²/g. The enhancement of specific surface area is due to the exfoliation of g-C₃N₄ sheets by the acid-assisted hydrothermal treatment [17] and/or results from the presence of in-plane pores and the crumpled layered structure [35]. Compared to bare g-C₃N₄, the hysteresis loops of FeGF2 become larger and shifts to a lower relative pressure, indicating the formation of enlarged mesopores during exfoliation [41]. The pore volumes of g-C₃N₄ and FeGF2 were calculated as 0.082 cm³/g and 0.427 cm³/g, respectively. The corresponding pore size distributions measured by BJH method are provided in the inset of Fig. 1(c). For both photocatalysts, pores are broadly distributed. The pore size distribution curve of FeGF2 shows a sharp peak at ~3.1 nm and a broad distribution in the range of 5–30 nm, which demonstrates that the micro/mesoporous structure of FeGF2 was well developed, while that of bare g-C₃N₄ has only negligible peaks. This dramatically increased the BET surface area, while the micro/mesoporous structure of FeGF2 should be beneficial for photocatalysis because it facilitates the mass transfer of reagents and the light harvesting by the multiple scattering effect. It also provides more catalytic active sites for photo-redox reaction compared to bare g-C₃N₄ [35,42]. The photocatalytic activity closely depends on the optical absorption ability of photocatalysts [27]. The UV-vis absorption spectra of g-C₃N₄, GF and FeGF composites are shown in Fig. 1(d). Clearly, all photocatalysts showed absorption in both UV and visible light region. Interestingly, fluorination enhanced the absorption in visible region and reduced the band gap from 2.7 eV to 2.52 eV compared to bare g-C₃N₄. The red shift of UV-vis spectrum by fluorination is different from protonation where g-C₃N₄ experienced a blue shift, suggesting that the process involved the

doping of fluorine into the C–N matrix rather than the physical surface adsorption of F[−] ions [22]. Moreover, the addition of Fe₃O₄ into the structure further increased the visible light absorption and strengthened the absorption intensity with the increase of Fe₃O₄ content. The higher light absorption of FeGF composites can be attributed to the intercalation effect of Fe₃O₄ nanoparticles which causes multiple absorption of reflected light in the interior space between layers [43]. Fig. 1(e) illustrates the band gap (E_g) calculation of samples. As shown, the E_g of g-C₃N₄ was 2.7 eV which is compatible with previous reports [22,44]. Due to the narrower E_g of Fe₃O₄, the band gap of FeGF composites decreased from 2.7 to ~2.3 eV for FeGF3. As shown in Fig. 1(f), the excited g-C₃N₄ sample showed a strong PL emission which is caused by recombination of charge carriers [16,43]. The strong PL emission behavior of g-C₃N₄ is consistent with previous studies [19,41]. The PL emission was significantly weakened in the case of GF by fluorination. Addition of Fe₃O₄ further reduced the PL emission. Nevertheless, compared to FeGF2, the FeGF3 sample showed a slightly higher PL emission. The reduction in PL peak intensity is associated with the charge carrier separation, which is beneficial for the enhancement of photocatalytic activity [41].

The XPS survey spectra and high-resolution spectra of FeGF2 elements are presented in Fig. 2. The survey spectra in Fig. 2(a) show that the FeGF2 sample is mainly composed of C and N elements, as expected. The high-resolution XPS spectra of C1s in Fig. 2(b) can be fitted into two peaks at 286.8 and 289.9 eV, corresponding to C–O from the adsorbed CO₂ [45] and 289.9 eV corresponding to N=C–N₂ coordination [25]. The high resolution of N1s (Fig. 2(c)) consists of three peaks at 398.6, 399.6 and 401.3 eV which are characteristics of C=N–C, (C₃)₂N

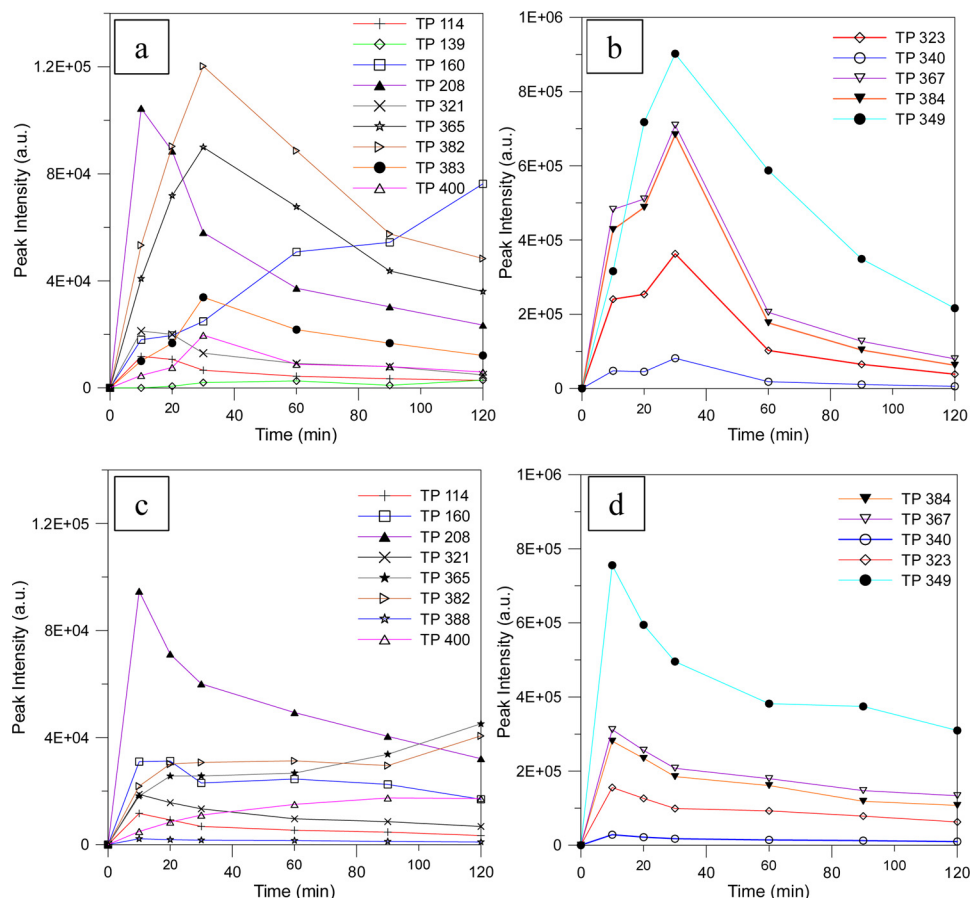


Fig. 7. Evolution of transformation products (TPs) with low (a), and high (b) peak intensities during the UV/g-C₃N₄ process; and with low (c), and high (d) peak intensities during the UV/FeGF2 process.

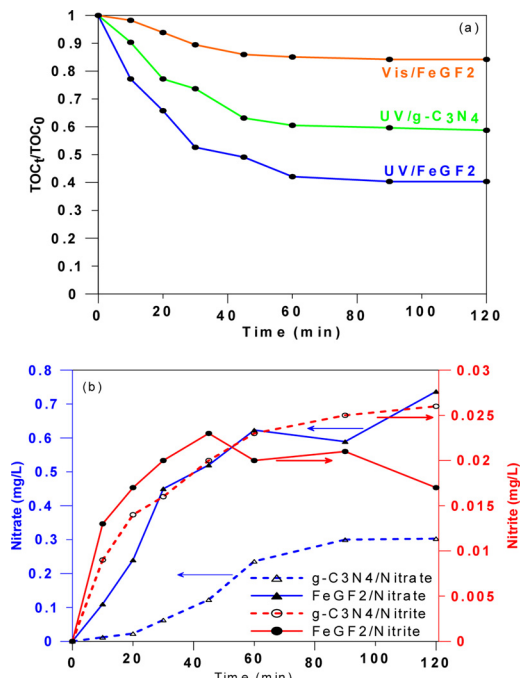


Fig. 8. (a) TOC removal during UV/g-C₃N₄, UV/FeGF2 and Vis/FeGF2 processes; (b) Evolution of nitrate and nitrite during UV/g-C₃N₄ and UV/FeGF2 processes.

and C–N–H, respectively [25]. In Fig. 2(d), two peaks located at 711.7 eV and 724.8 eV are attributed to Fe2p_{3/2} and Fe2p_{1/2}, respectively [46]. Because of the high electronegativity, fluorine is most certainly bound to carbon rather than to nitrogen [22]. As shown in Fig. 2(e), the peak at 686.2 eV of F1s spectra is attributed to the F–C bond [47]. The XPS peak at 686.2 eV and the FTIR band at 1220 cm^{−1} indicated that fluorine has been attached to C as the C–F bond rather than to other elements [22]. The weak peak at the binding energy of 692 eV is associated with CF₂ [48]. In Fig. 2(f), the three peaks of oxygen in the FeGF2 sample were attributed to O–Fe (530.1 eV), CO₃^{2−} (532.540 eV) and H–O–H (533.1 eV) [49]. The quantitative elemental analysis of FeGF2 obtained from the XPS analysis, is provided in Table S1.

3.2. Morphological analysis

The morphology of FeGF samples was investigated by the SEM techniques. As shown in Fig. S2(a–c), the FeGF1 sample shows aggregation of many wrinkled sheets with irregular shapes and pyramid-like structure and relatively smooth faces in certain parts. As seen in Fig. 3(a–c), the hydrothermal exfoliation of FeGF2 up to 180 °C changed a part of the sample to a curvy sheet as marked with arrows. The small particles of Fe₃O₄ are clearly observed on FeGF2 (Fig. 3(c)). However, as shown in Fig. S2(d–f), in the case of FeGF3, the Fe₃O₄ particles agglomerated on the GF, which reduces the active sites of the photocatalyst. The SEM images of FeGF1, FeGF3 and Fe₃O₄ at different magnifications are shown in Fig. S2. In addition, EDS mapping images of FeGF2 are presented in Fig. 3(d) where the N, C, O, Fe, and F elements are clearly detected, further confirming that the Fe₃O₄ particles have been deposited uniformly on the fluorinated g-C₃N₄.

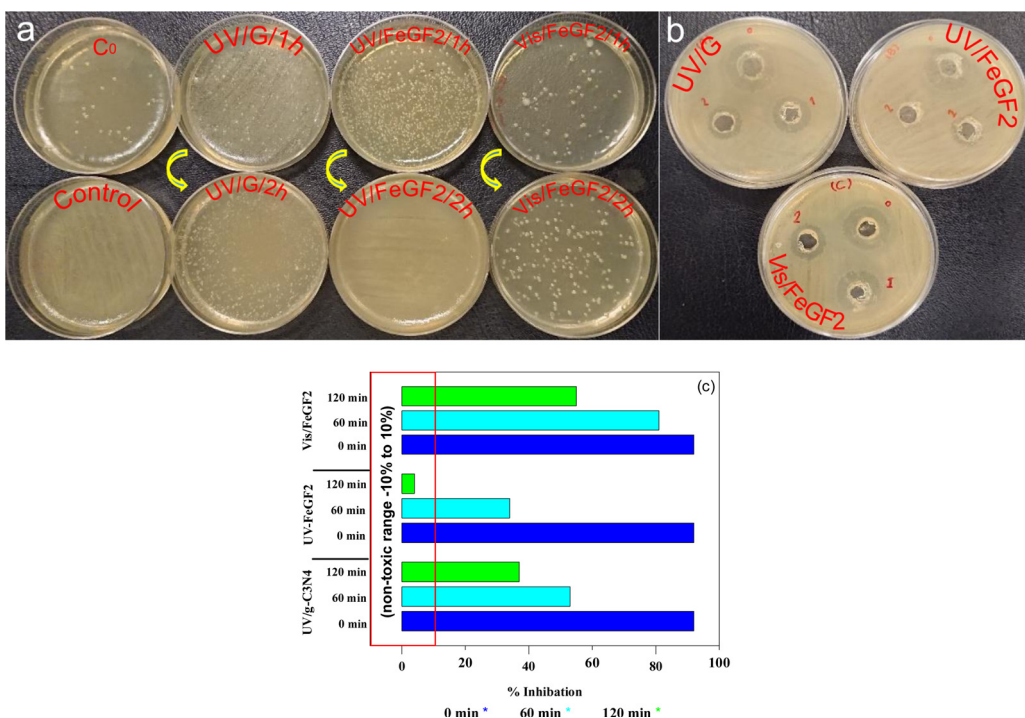


Fig. 9. Evaluation of changes in the toxicity of AMX solution by using (a) petri dish, (b) agar-well diffusion, and (c) inhibition percentage (Toxtrac™ kit) in UV/g-C₃N₄, UV/FeGF2 and Vis/FeGF2 processes.

Transmission electron microscopy (TEM) was employed to further examine the morphology of mesoporous FeGF2 (Fig. 4). A two-dimensional sheet-like structure consisting of wrinkles was observed in the FeGF2 sample which is similar to crumpled graphene [50]. Fig. 4(a) shows the distribution of Fe₃O₄ nanoparticles on the porous g-C₃N₄ sheets. The high resolution image of FeGF2 in Fig. 4(b) shows the decoration of Fe₃O₄, at the size of less than 30 nm, on the surface of g-C₃N₄ sheets. The porous structure of FeGF2 is clearly shown in Fig. 4(c). Fig. 4(d) shows the high angle annular dark field (HAADF) STEM image of FeGF2 sample. Since, in the HAADF the contrast of image is strongly dependent on the atomic number (Z) and number of atoms in a column (samples thickness) [51], this method has proven to be a powerful tool for the detection of compounds with different atomic number, thickness and porosity [52]. Accordingly, in Fig. 4(d), the bright spots in the high angle annular dark field (HAADF) STEM image show the decoration of Fe₃O₄ nanoparticles on g-C₃N₄ sheets, while the dark cores display the mesoporous structure.

3.3. Photocatalytic performance

As seen in Fig. 5(a), in the absence of photocatalysts, the AMX concentration was slightly reduced during the reaction course by photolysis. This is due to the low absorption of AMX molecules at the maximum emission intensity of low pressure UV lamp (Fig. S3). It has been reported that fluorination may change the adsorption capacity of photocatalysts towards organic compounds [53]. As shown in Fig. 5(a), the adsorption of AMX was slightly enhanced by fluorination. In addition, fluorination promotes the generation of mobile free ·OH radicals instead of surface bounded radicals [13]. Considering that the oxidation potential of mobile ·OH radicals (2.3 V vs NHE) is higher than that of attached surface radicals (1.5–1.7 V vs NHE), fluorination would increase the oxidation potential of ·OH radicals and removal efficiency of AMX. A significant enhancement of photocatalytic activity of g-C₃N₄ after fluorination for the oxidation of benzene to phenol has been reported [22]. Moreover, most photocatalytic reactions take place on the surface of photocatalysts and the application of fluorination changes

the kinetic and mechanism of reaction [13,54]. Fluorination, also led to a stable dispersion of photocatalyst in the solution which is beneficial for the photocatalytic process. As shown in Fig. S4, the GF particles were stable even after 24 h, while, the g-C₃N₄ particles precipitated after 30 min. It is worth noting that in this study, other parameters such as the specific surface area and adsorption capacity were enhanced simultaneously. Moreover, based on Fig. 1(f), the PL intensity which is an indicator of recombination of the excited electrons and holes was drastically reduced after fluorination. Although fluorination enhanced the AMX removal efficiency, the overall effects of fluorination on photocatalytic reactions are complex and need further investigation.

As shown in Fig. 5(a), the presence of Fe₃O₄ nanoparticles in the GF structure further enhanced the AMX removal efficiency. This improvement may be associated with the formation of heterojunction between Fe₃O₄ and GF. However, the photocatalytic activity of FeGF3 was reduced compared to FeGF2. In fact, the highest AMX removal was obtained by using the UV/FeGF2 process. The decline in photocatalytic activity may be caused by the excess Fe₃O₄ nanoparticles covering the photocatalyst active sites, thus producing a shielding effect [19,27]. Moreover, the excess amount of Fe₃O₄ in the photocatalyst can serve as the recombination center for electrons and holes [24] which is consistent with the slight enhancement of PL emission for FeGF3 in comparison with FeGF2 (Fig. 1(f)). The photocatalytic activity of FeGF2 for AMX removal was also evaluated under visible light. As shown in Fig. 5(a) the removal percentage of AMX by using visible light was lower than 40% even after 2 h treatment. The kinetic of AMX removal were studied by using the pseudo-first-order kinetics model:

$$-\ln\left(\frac{C_t}{C_0}\right) = kt \quad (3)$$

where C_0 and C_t (mM) are the initial and remaining AMX concentration at time t and k (min^{-1}) is the first-order rate constant. The rate constant for different photocatalysts under UV irradiation are shown in Fig. 5(b). FeGF2 exhibited the highest rate constant as $2.15 \times 10^{-2} \text{ min}^{-1}$. It is reported that hydroxyl radicals (·OH), photo-induced holes (h^+), and superoxide radicals (O_2^-) are the main reactive species during the

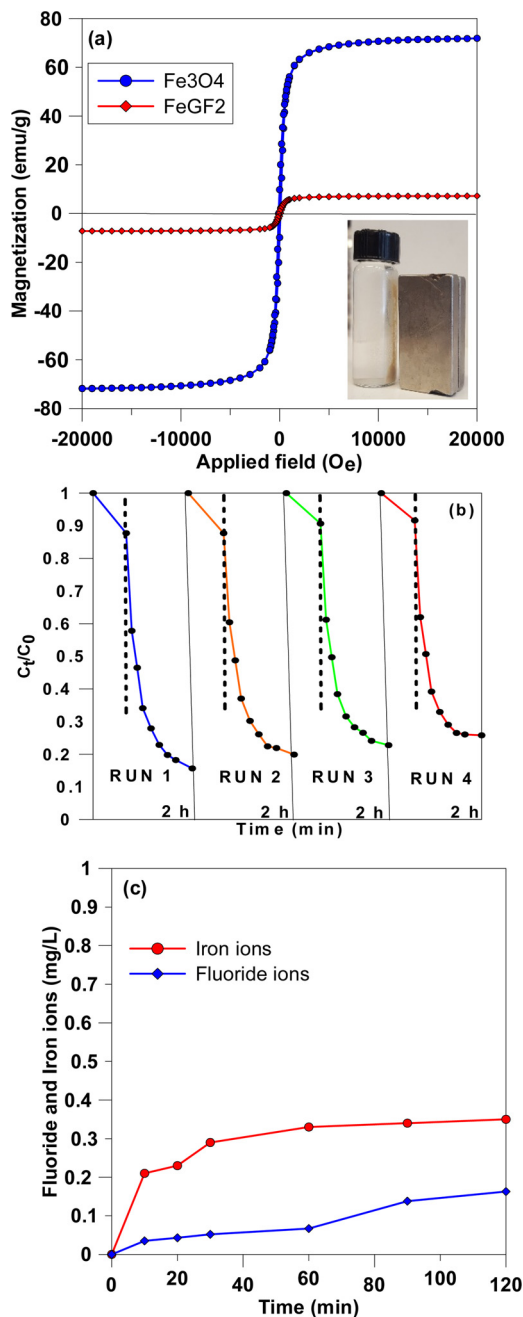
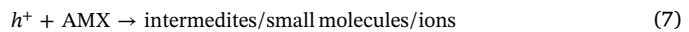


Fig. 10. (a) Magnetization curves of Fe₃O₄ and FeGF2, (b) repeated photocatalytic degradation of AMX by FeGF2 under UV irradiation, (c) fluoride and iron ions leaching from FeGF2 structure during UV/FeGF2 process.

photocatalytic degradation of organic pollutants [55]. Under the light irradiation, the excited FeGF2 will generate electrons and holes (Eq. (4)). Afterward, the photo-induced electrons rapidly move to the surface of FeGF2 and further to the Fe₃O₄ nanoparticles (Eq. (5)) [24]. These electrons can be subsequently transferred to dissolved oxygen and produce superoxide radicals (Eq. (6)). The produced holes can also participate in the direct oxidation of AMX and generate intermediates, by-products and/or ions (Eq. (7)). However, the redox ability of holes is not strong enough to generate hydroxyl radicals (+ 2.38 eV vs NHE for 'OH/OH⁻) [43]. Nevertheless, hydroxyl radicals may be produced in an indirect pathway (Eqs. (8) and (9)) [41].



Accordingly, experiments were conducted in the presence of 2.5 mM TBA, EDTA, and BQ as scavenger of 'OH, h⁺ and 'O²⁻ species, respectively. As shown in Fig. 5(c), the highest inhibition effect was observed when EDTA was added to the reaction, followed by TBA and BQ, respectively. Therefore, holes play an important role in the photocatalytic degradation of AMX by FeGF2 under UV irradiation, followed by hydroxyl and superoxide radicals. The dominant role of holes in AMX removal is consistent with the observations of Yang et al. [56] for the degradation of AMX. The presence of fluorine, which is the most electronegative element, on the surface of photocatalyst reduces the formation and contribution of 'O²⁻ by holding the electrons [13,57], while promoting the role of holes as strong species which can oxidize AMX or the generated intermediates on the surface of FeGF2 which has a high surface area.

3.4. Identification of intermediates and AMX degradation pathway

The identification of main transformation products (TPs) formed during the UV/g-C₃N₄ and UV/FeGF2 processes was conducted in an effort to propose a pathway for AMX degradation and to identify the potential intermediate compounds and by-products that may contribute to the solution toxicity (Fig. 6). The employed analytical methods allowed the detection of thirteen intermediate compounds during the degradation of AMX by the UV/FeGF2 process, and fourteen intermediates during its degradation by the UV/g-C₃N₄ process. The first possible pathway is the hydroxylation (+ 16 Da) of AMX which may occur at different positions of the AMX molecule such as benzoic ring or nitrogen moiety (TP 382). The identification of the exact position of hydroxylation on the AMX molecule is difficult by solely relying on the employed method of analysis. However, almost all detected intermediates consisted of the thiazolidine ring (C₆H₁₀NO₂S) and fragment [m/z = 160.04] in their mass spectrum (data is not shown), suggesting that the thiazolidine ring of AMX is not susceptible to hydroxylation. This observation suggests that the benzoic ring or amine group of AMX which possess electrophilic characteristics is more prone to radical attack. Nevertheless, the presence of [m/z = 189.06] fragment which corresponds to the C₇H₁₃N₂O₂S formula (see Fig. S5) implies that the 'OH radical most likely attached to nitrogen rather than to the benzoic ring. This intermediate can further lose the amine moiety and produce TP 365. Another possible transformation pathway involves the loss of amine group of AMX which leads to the formation of TP 349. The detection of TP 349 has been reported in the literature [2,58], and showed the highest peak intensity in both UV/g-C₃N₄ and UV/FeGF2 processes. The loss of C=O from four-membered β-lactam ring of TP 349 produces TP 321 which is detected in both processes with lower peak intensities compared to TP 349. However, the hydroxylation product of TP 349 which led to the formation of TP 383 was only detected in the UV/g-C₃N₄ process. Moreover, as seen in Fig. S6, the detection of [m/z = 155.015] fragment suggests that 'OH radical most likely attached to both benzoic ring and nitrogen moiety rather than to benzoic ring alone. The opening of the four-membered β-lactam ring of the AMX is another possible degradation pathway which was also reported before [59]. This degradation pathway yielded the formation of AMX penicilloic acid (TP 384) [2]. The hydroxylation of AMX penicilloic acid produces the TP 400 which can further be transformed by losing amine and CO₂ groups, resulting in the formation of TP 323. The loss of amine group and the removal of β-lactam ring are two probable

means of producing by-products from AMX penicilloic acid with the subsequent production of **TP 367** and AMX penilloic acid (**TP 340**), respectively, in accordance with the observations of Pe'rez-Parada et al. [60]. The intermediates formed by the opening of the four-membered β -lactam ring of AMX were detected at higher peak intensities in both processes compared to TPs with β -lactam ring. Amoxicillin sodium (**TP 388**) was also detected with very low peak intensities only in the UV/FeGF2 process, and its peak intensity was reduced during the reaction course. As shown in Fig. 7(a–b) the peak intensity of most transformation products increased up to 30 min in the UV/g-C₃N₄ process and then decreased with the progress of the process. The long chain products possibly broke into short chain compounds such as **TP 208**, **TP 160** and **TP 114**. As seen in Fig. 7(c–d) the intensity of intermediates during the UV/FeGF2 process was considerably lower than those in the UV/g-C₃N₄ process. Moreover, the reduction in peak intensity was shown after 10 min for most compounds. The **TP 139** with low peak intensity was also detected during the UV/FeGF2 process. Further oxidation of intermediates led to the mineralization of compounds in the solution and the generation of ions such as nitrate and nitrite.

3.5. Mineralization

The removal of total organic carbon (TOC) as well as the formation of nitrate and nitrite as indicators of mineralization were evaluated. As shown in Fig. 8(a), all examined processes showed some extent of AMX mineralization. However, the UV/FeGF2 process with almost 60% TOC removal after 2 h showed the highest efficiency for the mineralization of AMX, followed by the UV/g-C₃N₄ and Vis/FeGF2 processes with 42% and 16%, respectively. Fig. 8 shows that the mineralization rate was relatively high during the first 30 min of the photocatalytic process and then decreased as the process proceeded. The intermediate compounds formed during the examined processes may also be more resistant to further degradation as observed before during the photocatalytic degradation of AMX by the UV/TiO₂ process [2]. The presence of sulfur in most detected TPs indicates that nitrogen and amine moiety are more susceptible to radical attack compared to sulfur. Therefore, the formation of nitrate and nitrite were monitored as indicators of mineralization. As seen in Fig. 8(b), during the UV/g-C₃N₄ and UV/FeGF2 processes, the concentration of nitrate and nitrite increased as the process progressed. However, the concentration of nitrate produced by the UV/FeGF2 process was considerably higher than that formed by the UV/g-C₃N₄ process. The concentrations of nitrate and nitrite during the Vis/FeGF2 process were consistently lower than the detection limit of employed measurement techniques.

3.6. Toxicity assessment

As shown in Fig. 8, total mineralization was not achieved during the photocatalytic experiments even after 2 h. Therefore, toxicity assays using *E. coli* bacteria were conducted to evaluate the antibiotic activity prior and after the treatment operations. As seen in Fig. 9(a), the AMX solution before treatment significantly inhibited the growth of *E. coli* on the surface of agar, while bacterial growth was clearly observed after the onset of photocatalytic processes. Since no inhibition was detected in the control plate, the observed changes in bacterial growth were attributed to AMX degradation. As shown by the UV/G petri dishes in Fig. 9(a), the bare g-C₃N₄ was relatively effective for the detoxification of solution under UV light after 1 and 2 h of treatment. However, this process was not able to totally suppress the antibacterial activity of AMX solution. The FeGF2 photocatalyst was also examined for the detoxification of AMX solution. The results showed that although the Vis/FeGF2 process was relatively effective, it did not produce a complete detoxification of solution. On the other hand, a complete detoxification, identified by the reduction of toxicity below the minimum inhibitory level for *E. coli*, was obtained by employing UV light during the UV/FeGF2 process (see UV/FeGF2/2 h plate in Fig. 9(a)).

These results were also confirmed by the agar-well diffusion method. As shown in Fig. 9(b), by using FeGF2 in the presence of UV light, the diameter of inhibition zone was reduced after 1 h and eventually disappeared after 2 h treatment. However, under visible light, an inhibition zone still existed even after 2 h treatment. Fig. 9(c) shows the percentage inhibition (PI) of solution by the UV/g-C₃N₄, UV/FeGF2 and Vis/FeGF2 processes at two time intervals. A high inhibition percentage of AMX solution towards *E. coli* growth was shown before the treatment. One hour treatment of solution reduced the inhibition percentage from 92% to 53%, 34% and 81% by the UV/g-C₃N₄, UV/FeGF2 and Vis/FeGF2 processes, respectively. The increase of treatment time up to 120 min decreased the toxicity of solution in all processes. However, only the solutions treated by the UV/FeGF2 process exhibited toxicity levels within the non-toxic range, indicating the effectiveness of UV/FeGF2 process in the reduction of toxicity.

3.7. Stability of photocatalyst

The stability and recyclability of a photocatalyst are of great importance for its application [41]. The magnetic properties of Fe₃O₄ and FeGF2 samples were investigated at room temperature and the results are presented in Fig. 10(a). The hysteresis loop in both samples indicates a superparamagnetic behavior without any noticeable remanence. Due to the low percentage of Fe₃O₄ in the FeGF2, the saturation magnetization of FeGF2 was lower than bare Fe₃O₄. Nevertheless, the magnetic properties of FeGF2 were high enough to enable its separation from the treated solution by magnetic force (Inset of Fig. 10(a)). The FeGF2 particles were found to be highly stable and could be reused in repeated operational runs without a significant reduction in their activity. The high stability of photocatalyst is also confirmed by XPS spectra of fresh and spent FeGF2 (Fig. S7).

As shown in Fig. 10(b), no noticeable reduction in AMX removal was observed after four cyclic operations, which indicates the high stability of photocatalyst particles.

Moreover, the concentrations of fluoride and iron ions during the reaction course were measured in order to assess possible leaching of fluoride and iron ions from the photocatalysts that may reduce the photocatalyst activity. The monitoring of fluoride ion concentration in the treated water is also important since concentrations up to 1.5 mg/L fluoride is beneficial, especially to children for calcification of dental enamel [61], while prolonged exposure to F[–] ion at higher concentrations leads to dental and skeletal fluorosis [62]. A maximum concentration of 1.5 mg/L of fluoride ion in drinking water has been set as the limit by World Health Organization (WHO) [63]. As shown in Fig. 10(c), after 120 min process, the concentration of F[–] was about 0.16 mg/L, which was considerably lower than the permitted concentration. These results further verify the high stability of FeGF2 photocatalyst.

4. Conclusion

Herein, we have shown a simple exfoliation and fluorination route for the formation of mesoporous g-C₃N₄ photocatalyst with magnetic properties. A high efficiency for the photocatalytic removal of AMX by the UVC lamp irradiation has been achieved by the FeGF2 photocatalyst. The improved photocatalyst activity of FeGF2 compared to g-C₃N₄ is attributed to the following four reasons: (1) exfoliation and porous structure of FeGF2 photocatalyst, which offered a high specific surface area and a stable dispersity; (2) presence of Fe₃O₄ in the structure of photocatalyst, which facilitated charge transfer and reduced the recombination of charged electrons and holes, in addition to the convenient separation of FeGF2 from the solution; (3) higher absorption of UV and visible light as a result of exfoliation and utilization of reflected light between layers; and (4) use of cylindrical photoreactor with an immersed lamp, which enhanced the utilization of light. Although FeGF2 exhibited photocatalytic activity under both UV and

visible lights, the efficiency of AMX degradation process by using a 10 W UV lamp was significantly higher than that observed under a 500 W visible light lamp in terms of AMX removal and mineralization and solution detoxification. Based on the measurement of accurate masses of the transformation products and their main fragments, a pathway for the degradation of AMX was proposed. The FeGF2 particles were easily separated from the treated solution and they were shown to be stable after five cyclic operations.

Appendix A. Supplementary data

Supplementary material related to this article can be found, in the online version, at doi:<https://doi.org/10.1016/j.apcatb.2018.10.009>.

References

- M. Wang, L. Zhang, G. Zhang, T. Pang, X. Zhang, D. Cai, Z. Wu, In situ degradation of antibiotic residues in medical intravenous infusion bottles using high energy electron beam irradiation, *Sci. Rep.* 7 (2017) 39928.
- D. Kanakaraju, J. Kockler, C.A. Motti, B.D. Glass, M. Oelgemöller, Titanium dioxide/zeolite integrated photocatalytic adsorbents for the degradation of amoxicillin, *Appl. Catal. B: Environ.* 166 (2016) 45–55.
- A. Mirzaei, Z. Chen, F. Haghishat, L. Yerushalmi, Removal of pharmaceuticals from water by homo/heterogeneous Fenton-type processes—a review, *Chemosphere* 174 (2017) 665–688.
- R. Andreozzi, V. Caprio, C. Ciniglia, M. de Champdoré, R. Lo Giudice, R. Marotta, E. Zuccato, Antibiotics in the environment: occurrence in Italian STPs, fate, and preliminary assessment on algal toxicity of amoxicillin, *Environ. Sci. Technol.* 38 (2004) 6832–6838.
- M. Pourakbar, G. Moussavi, S. Shekohiyan, Homogenous UVV advanced oxidation process for enhanced degradation and mineralization of antibiotics in contaminated water, *Ecotoxicol. Environ. Saf.* 125 (2016) 72–77.
- M. Gmurek, M. Bizukojć, J. Mosinger, S. Ledakowicz, Application of photoactive electrospun nanofiber materials with immobilized meso-tetraphenylporphyrin for parabens photodegradation, *Catal. Today* 240 (2015) 160–167.
- V. Singh, B. Pandey, S. Suthar, Phytotoxicity of amoxicillin to the duckweed *Spirodela polyrhiza*: growth, oxidative stress, biochemical traits and antibiotic degradation, *Chemosphere* 201 (2018) 492–502.
- N.A. Alygizakis, P. Gago-Ferrero, V.L. Borova, A. Pavlidou, I. Hatzianestis, N.S. Thomaidis, Occurrence and spatial distribution of 158 pharmaceuticals, drugs of abuse and related metabolites in offshore seawater, *Sci. Total Environ.* 541 (2016) 1097–1105.
- Q. Zheng, D.P. Durkin, J.E. Elenewski, Y. Sun, N.A. Banek, L. Hua, H. Chen, M.J. Wagner, W. Zhang, D. Shuai, Visible-light-responsive graphitic carbon nitride: rational design and photocatalytic applications for water treatment, *Environ. Sci. Technol.* 50 (2016) 12938–12948.
- S. Liu, Q. Hu, J. Qiu, F. Wang, W. Lin, F. Zhu, C. Wei, N. Zhou, G. Ouyang, Enhanced photocatalytic degradation of environmental pollutants under visible irradiation by a composite coating, *Environ. Sci. Technol.* 51 (2017) 5137–5145.
- M. Bahri, A. Mahdavi, A. Mirzaei, A. Mansouri, F. Haghishat, Integrated oxidation process and biological treatment for highly concentrated petrochemical effluents: a review, *Chem. Eng. Process.—Process Intensif.* 125 (2018) 183–196.
- A. Mirzaei, Z. Chen, F. Haghishat, L. Yerushalmi, Hierarchical magnetic petal-like Fe3O4-ZnO@g-C3N4 for removal of sulfamethoxazole, suppression of photocorrosion, by-products identification and toxicity assessment, *Chemosphere* 205 (2018) 463–474.
- A. Mirzaei, L. Yerushalmi, Z. Chen, F. Haghishat, J. Guo, Enhanced photocatalytic degradation of sulfamethoxazole by zinc oxide photocatalyst in the presence of fluoride ions: optimization of parameters and toxicological evaluation, *Water Res.* 132 (2018) 241–251.
- Z. Shayegan, C.-S. Lee, F. Haghishat, TiO2 photocatalyst for removal of volatile organic compounds in gas phase—a review, *Chem. Eng. J.* 334 (2018) 2408–2439.
- A. Mirzaei, Z. Chen, F. Haghishat, L. Yerushalmi, Removal of pharmaceuticals and endocrine disrupting compounds from water by zinc oxide-based photocatalytic degradation: a review, *Sustain. Cities Soc.* 27 (2016) 407–418.
- S. Zhang, J. Li, M. Zeng, G. Zhao, J. Xu, W. Hu, X. Wang, In situ synthesis of water-soluble magnetic graphitic carbon nitride photocatalyst and its synergistic catalytic performance, *ACS Appl. Mater. Interfaces* 5 (2013) 12735–12743.
- S. Zhang, J. Li, X. Wang, Y. Huang, M. Zeng, J. Xu, In situ ion exchange synthesis of strongly coupled Ag@AgCl/g-C3N4 porous nanosheets as plasmonic photocatalyst for highly efficient visible-light photocatalysis, *ACS Appl. Mater. Interfaces* 6 (2014) 22116–22125.
- X. Wang, K. Maeda, A. Thomas, K. Takane, G. Xin, J.M. Carlsson, K. Domen, M. Antonietti, A metal-free polymeric photocatalyst for hydrogen production from water under visible light, *Nat. Mater.* 8 (2009) 76–80.
- Y. He, L. Zhang, B. Teng, M. Fan, New application of Z-scheme Ag3PO4/g-C3N4 composite in converting CO2 to fuel, *Environ. Sci. Technol.* 49 (2014) 649–656.
- J. Xiao, Q. Han, Y. Xie, J. Yang, Q. Su, Y. Chen, H. Cao, Is C3N4 chemically stable toward reactive oxygen species in sunlight-driven water treatment? *Environ. Sci. Technol.* 51 (2017) 13380–13387.
- L. Ge, C. Han, J. Liu, Y. Li, Enhanced visible light photocatalytic activity of novel polymeric gC3N4 loaded with Ag nanoparticles, *Appl. Catal. A: Gen.* 409 (2011) 215–222.
- Y. Wang, Y. Di, M. Antonietti, H. Li, X. Chen, X. Wang, Excellent visible-light photocatalysis of fluorinated polymeric carbon nitride solids, *Chem. Mater.* 22 (2010) 5119–5121.
- Y. Wang, J. Zhang, X. Wang, M. Antonietti, H. Li, Boron-and fluorine-containing mesoporous carbon nitride polymers: metal-free catalysts for cyclohexane oxidation, *Angew. Chem. Int. Ed.* 49 (2010) 3356–3359.
- X. Zhou, B. Jin, R. Chen, F. Peng, Y. Fang, Synthesis of porous Fe3O4/g-C3N4 nanospheres as highly efficient and recyclable photocatalysts, *Mater. Res. Bull.* 48 (2013) 1447–1452.
- K.H. Leong, S.L. Liu, L.C. Sim, P. Saravanan, M. Jang, S. Ibrahim, Surface reconstruction of titania with g-C3N4 and Ag for promoting efficient electrons migration and enhanced visible light photocatalysis, *Appl. Surf. Sci.* 358 (2015) 370–376.
- X. Wang, A. Wang, J. Ma, Visible-light-driven photocatalytic removal of antibiotics by newly designed C3N4@MnFe2O4-graphene nanocomposites, *J. Hazard. Mater.* 336 (2017) 81–92.
- D. Zhu, S. Liu, M. Chen, J. Zhang, X. Wang, Flower-like-flake Fe3O4/g-C3N4 nanocomposite: facile synthesis, characterization, and enhanced photocatalytic performance, *Colloids Surf. A: Physicochem. Eng. Aspects* 537 (2018) 372–382.
- O.A. Alsager, M.N. Alnajrani, O. Alhazza, Decomposition of antibiotics by gamma irradiation: kinetics, antimicrobial activity, and real application in food matrices, *Chem. Eng. J.* 338 (2018) 548–556.
- L. Hou, L. Wang, S. Royer, H. Zhang, Ultrasound-assisted heterogeneous Fenton-like degradation of tetracycline over a magnetite catalyst, *J. Hazard. Mater.* 302 (2016) 458–467.
- S. Shen, D. Zhao, J. Chen, L. Guo, S.S. Mao, Enhanced photocatalytic hydrogen evolution over graphitic carbon nitride modified with Ti-activated mesoporous silica, *Appl. Catal. A: Gen.* 521 (2016) 111–117.
- Y. Zhao, F. Zhao, X. Wang, C. Xu, Z. Zhang, G. Shi, L. Qu, Graphitic carbon nitride nanoribbons: graphene-assisted formation and synergic function for highly efficient hydrogen evolution, *Angew. Chem. Int. Ed.* 53 (2014) 13934–13939.
- Q. Han, B. Wang, J. Gao, Z. Cheng, Y. Zhao, Z. Zhang, L. Qu, Atomically thin mesoporous nanosheet of graphitic C3N4 for high-efficiency photocatalytic hydrogen evolution, *ACS Nano* 10 (2016) 2745–2751.
- C. Dong, Z. Ma, R. Qie, X. Guo, C. Li, R. Wang, Y. Shi, B. Dai, X. Jia, Morphology and defect regulation of carbon nitride by hydrochloric acid to boost visible light absorption and photocatalytic activity, *Appl. Catal. B: Environ.* 217 (2017) 629–636.
- T.Y. Ma, Y. Tang, S. Dai, S.Z. Qiao, Proton-Functionalized two-dimensional graphitic carbon nitride nanosheet: an excellent metal-/label-free biosensing platform, *Small* 10 (2014) 2382–2389.
- L. Shi, K. Chang, H. Zhang, X. Hai, L. Yang, T. Wang, J. Ye, Drastic enhancement of photocatalytic activities over phosphoric acid protonated porous g-C3N4 nanosheets under visible light, *Small* 12 (2016) 4431–4439.
- Y. Wang, X. Bai, C. Pan, J. He, Y. Zhu, Enhancement of photocatalytic activity of Bi 2 WO 6 hybridized with graphite-like C3N4, *J. Mater. Chem.* 22 (2012) 11568–11573.
- L. Ge, F. Zuo, J. Liu, Q. Ma, C. Wang, D. Sun, L. Bartels, P. Feng, Synthesis and efficient visible light photocatalytic hydrogen evolution of polymeric g-C3N4 coupled with CdS quantum dots, *J. Phys. Chem. C* 116 (2012) 13708–13714.
- S. Yan, Z. Li, Z. Zou, Photodegradation performance of g-C3N4 fabricated by directly heating melamine, *Langmuir* 25 (2009) 10397–10401.
- M. Xie, W. Wei, Z. Jiang, Y. Xu, J. Xie, Carbon nitride nanowires/nanofibers: a novel template-free synthesis from a cyanuric chloride-melamine precursor towards enhanced adsorption and visible-light photocatalytic performance, *Ceram. Int.* 42 (2016) 4158–4170.
- X. Tang, L. Ni, J. Han, Y. Wang, Preparation and characterization of ternary magnetic g-C3N4 composite photocatalysts for removal of tetracycline under visible light, *Chin. J. Catal.* 38 (2017) 447–457.
- F. Dong, Z. Wang, Y. Li, W.-K. Ho, S. Lee, Immobilization of polymeric g-C3N4 on structured ceramic foam for efficient visible light photocatalytic air purification with real indoor illumination, *Environ. Sci. Technol.* 48 (2014) 10345–10353.
- Y. Gui, J. Huang, X. Fu, X. Wang, Metal-free photocatalytic degradation of 4-chlorophenol in water by mesoporous carbon nitride semiconductors, *Catal. Sci. Technol.* 2 (2012) 1396–1402.
- Z. Zhu, Y. Yu, H. Dong, Z. Liu, C. Li, P. Huo, Y. Yan, Intercalation effect of attapulgite in g-C3N4 modified with Fe3O4 quantum dots to enhance photocatalytic activity for removing 2-mercaptopbenzothiazole under visible light, *ACS Sustain. Chem. Eng.* 5 (2017) 10614–10623.
- X. Miao, X. Shen, J. Wu, Z. Ji, J. Wang, L. Kong, M. Liu, C. Song, Fabrication of an all solid Z-scheme photocatalyst g-C3N4/GO/AgBr with enhanced visible light photocatalytic activity, *Appl. Catal. A: Gen.* 539 (2017) 104–113.
- B. Zhu, P. Xia, W. Ho, J. Yu, Isoelectric point and adsorption activity of porous g-C3N4, *Appl. Surf. Sci.* 344 (2015) 188–195.
- Z. Dong, Y. Wu, Magnetically separable photocatalyst of direct Z-scheme g-C3N4 nanosheets/natural hematite ore hybrids, *J. Photochem. Photobiol. A: Chem.* 336 (2017) 156–163.
- J. Zha, S.S. Ali, J. Peyroux, N. Batisse, D. Claves, M. Dubois, A.P. Kharitonov, G. Monier, T. Darmanin, F. Guittard, Superhydrophobicity of polymer films via fluorine atoms covalent attachment and surface nano-texturing, *J. Fluorine Chem.* 200 (2017) 123–132.
- C. Struzzi, M. Scardamaglia, N. Reckinger, J.-F. Colomer, H. Sezen, M. Amati, L. Gregoratti, R. Snyders, C. Bittencourt, Fluorination of suspended graphene, *Nano Res.* 10 (2017) 3151–3163.
- H.-Y. Jiang, G. Liu, T. Wang, P. Li, J. Lin, J. Ye, In situ construction of α -Bi2O3/

gC₃N₄/β-Bi₂O₃ composites and their highly efficient photocatalytic performances, RSC Adv. 5 (2015) 92963–92969.

[50] J. Luo, X. Zhao, J. Wu, H.D. Jang, H.H. Kung, J. Huang, Crumpled graphene-encapsulated Si nanoparticles for lithium ion battery anodes, *J. Phys. Chem. Lett.* 3 (2012) 1824–1829.

[51] Z. Li, N. Young, M. Di Vece, S. Palomba, R. Palmer, A. Bleloch, B. Curley, R. Johnston, J. Jiang, J. Yuan, Three-dimensional atomic-scale structure of size-selected gold nanoclusters, *Nature* 451 (2008) 46.

[52] R. Leary, Z. Saghi, M. Armbrester, G. Wownick, R. Schlägl, J.M. Thomas, P.A. Midgley, quantitative high-angle annular dark-field scanning transmission electron microscope (HAADF-STEM) tomography and high-resolution electron microscopy of unsupported intermetallic GaPd₂ catalysts, *J. Phys. Chem. C* 116 (2012) 13343–13352.

[53] S. Liu, J. Yu, B. Cheng, M. Jaroniec, Fluorinated semiconductor photocatalysts: tunable synthesis and unique properties, *Adv. Colloid Interface Sci.* 173 (2012) 35–53.

[54] A. Mirzaei, Z. Chen, F. Haghigheh, L. Yerushalmi, Enhanced adsorption of anionic dyes by surface fluorination of zinc oxide: a straightforward method for numerical solving of the ideal adsorbed solution theory (IAST), *Chem. Eng. J.* 330 (2017) 407–418.

[55] S. Cao, J. Low, J. Yu, M. Jaroniec, Polymeric photocatalysts based on graphitic carbon nitride, *Adv. Mater.* 27 (2015) 2150–2176.

[56] C. Yang, X. You, J. Cheng, H. Zheng, Y. Chen, A novel visible-light-driven in-based MOF/graphene oxide composite photocatalyst with enhanced photocatalytic activity toward the degradation of amoxicillin, *Appl. Catal. B: Environ.* 200 (2017) 673–680.

[57] J. Yu, W. Wang, B. Cheng, B.-L. Su, Enhancement of photocatalytic activity of mesporous TiO₂ powders by hydrothermal surface fluorination treatment, *J. Phys. Chem. C* 113 (2009) 6743–6750.

[58] I. Gozlan, A. Rotstein, D. Avisar, Amoxicillin-degradation products formed under controlled environmental conditions: identification and determination in the aquatic environment, *Chemosphere* 91 (2013) 985–992.

[59] A.G. Trovo, R.F.P. Nogueira, A. Agüera, A.R. Fernandez-Alba, S. Malato, Degradation of the antibiotic amoxicillin by photo-Fenton process-chemical and toxicological assessment, *Water Res.* 45 (2011) 1394–1402.

[60] A. Pérez-Parada, A. Agüera, Md.M. Gómez-Ramos, J.F. García-Reyes, H. Heinzen, A.R. Fernández-Alba, Behavior of amoxicillin in wastewater and river water: identification of its main transformation products by liquid chromatography/electrospray quadrupole time-of-flight mass spectrometry, *Rapid Commun. Mass Spectrom.* 25 (2011) 731–742.

[61] M. Srimurali, A. Pragathi, J. Karthikeyan, A study on removal of fluorides from drinking water by adsorption onto low-cost materials, *Environ. Pollut.* 99 (1998) 285–289.

[62] M. Mohapatra, S. Anand, B.K. Mishra, D.E. Giles, P. Singh, Review of fluoride removal from drinking water, *J. Environ. Manage.* 91 (2009) 67–77.

[63] WHO, Guidelines for Drinking Water Quality, Geneva, (2004).